CHEMISTRY OF MATERIALS

Article

pubs.acs.org/cm

Microstructural 3D Reconstruction and Performance Evaluation of LSCF Cathodes Obtained by Electrostatic Spray Deposition

Daniel Marinha,[†] Laurent Dessemond,[†] J. Scott Cronin,[‡] James R. Wilson,[‡] Scott A. Barnett,[‡] and Elisabeth Djurado*[,†]

[†]Laboratoire d'Electrochimie et de Physico-Chimie des Matériaux et des Interfaces, LEPMI, UMR 5279, CNRS-Grenoble INP-Université de Savoie-Université Joseph Fourier BP75, 38402 Saint Martin d'Hères, France

[‡]Department of Materials Science and Engineering, Northwestern University, 2220 Campus Drive, Evanston, Illinois 60208, United States

ABSTRACT: Electrostatic spray deposition (ESD) was used to deposit $La_{0.6}Sr_{0.4}Co_{0.2}Fe_{0.8}O_{3-\delta}$ (LSCF) cathode films on dense $Ce_{0.9}Gd_{0.1}O_{2-\delta}$ (CGO) electrolytes. LSCF films with different morphologies were obtained by varying the substrate temperature (250 to 450 °C), nozzle-to-substrate distance (15−45 mm) and precursor solution flow rate (0.34 to 1.5 mL h^{-1}). A detailed study on the influence of the microstructure of LSCF cathode films on electrochemical behavior is reported. Resulting films can be classified according to their morphology as dense, cracked and coral microstructures. Detailed microstructural characterization was made by SEM and completed with 3D focused ion beam−scanning electron beam (FIB-SEM) tomography of representative samples. Surface areas of the cathode/pore interfaces, normalized by the cross-sectional area of the support, were found to be 2.0, 24.7, and 28.2 for dense, cracked and coral microstructures, respectively. Electrical measurements were performed at intermediate temperatures (400−600 °C) by AC impedance spectroscopy in air. Area specific polarization resistance, R_{pol}, values ranged from 6.23 to 0.82 Ω cm^2, with lower values corresponding to samples with higher surface areas. Up to three elementary steps were identified in the oxygen reduction reaction of these films. Microstructural parameters determined by FIB-SEM analysis were used to model the electrical performance of the different cathodes, in good agreement with experimental impedance data.

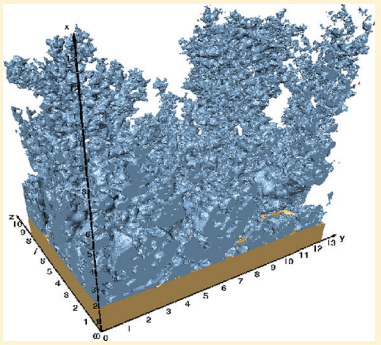

KEYWORDS: *SOFC, LSCF, electrostatic spray deposition, ESD, impedance spectroscopy, MIEC, 3D, FIB-SEM, tomography*

INTRODUCTION

There is great interest in reduced temperature SOFCs operating below 700 °C (IT-SOFCs) for numerous reasons including a reduction of operation costs and mechanical fatigue of materials leading to an enhancement of the cell durability. However, a key barrier in achieving reasonable performances from IT-SOFCs relies on the cathode material, which is responsible for the highest percentage of voltage losses in the cell. Elementary processes occurring on the cathode are functions of its (i) electronic and ionic conductivities, (ii) solid/gas interfacial area, (iii) charge-transfer reaction rate at the solid/gas interface, and (iv) charge-transfer reaction rate at the cathode/electrolyte interface. This implies that the global process efficiency is strictly related to the intrinsic transport properties of the material, as well as to its microstructure. Mixed-ionic electronic (MIEC) materials such as $La_{0.6}Sr_{0.4}Co_{0.2}Fe_{0.8}O_{3-\delta}$ (LSCF) are an important class of cathodes due to relatively high transport properties[1,2] and catalytic activity toward oxygen reduction.[3,4] A number of different methods[5−8] have been used to fabricate MIEC cathodes. The fabrication process is important to produce a microstructure with high surface area, which helps to yield low polarization resistance values,[9−11] as described in the Adler−Lane−Steel (ALS) model.[12]

In this report, we describe such a simple and low-cost method for cathode fabrication, electrostatic spray deposition (ESD) and demonstrate its applicability to LSCF cathodes. The effect of different process parameters on the resulting microstructure and consequently on R_{pol} are detailed. In ESD, a strong electrical field applied between a nozzle and a substrate is used to generate an aerosol from a precursor solution being pumped at a controlled flow rate through the nozzle. The physicochemical properties of the precursor solution and the deposition parameters such as flow rate, substrate temperature, or the distance between the nozzle and the substrate, all play a role in determining the average droplet size in the aerosol,[13] which ultimately determines the morphology of the layer being deposited. ESD allows fabrication of highly adherent films to be deposited with the most varied morphologies by controlling a very limited number of parameters.[14,15] The cathodes were deposited onto $Ce_{0.9}Gd_{0.1}O_{2-\delta}$ (CGO) substrates and ESD parameters were varied to obtain different film morphologies. R_{pol} was determined by impedance spectroscopy and compared with ALS model prediction informed by 3D microstructural

Received: June 15, 2011
Revised: October 25, 2011
Published: November 22, 2011

Table 1. Summary of the Sample Deposition Conditions: Substrate Temperature, *T*; Solution Flow Rate, *Q*; Nozzle-to-Substrate Distance, *d*; Deposition Time, *t*; Voltage, *V*[a]

microstructure	sample	*T* (°C)	Q (mL h^{-1})	*d* (mm)	*t* (h)	*V* (kV)	precursor solution	film thickness (μm)
dense	D1	300	1.59	25	1	8 - 10	A	3−4
	D2	300	1.59	30	1	8 - 10	A	2−3
	D3	300	1.59	35	1	8 - 10	A	1−2
cracked	Cr1	300	1.59	20	1	8 - 10	A	3−4
	Cr2	350	1.59	15	1	6 - 8	A	7−8
	Cr3	300	1.5	15	1.5	6	A	7−8
coral	Co1	300/450	0.4/1.59	30/58	1 + 2	6 - 10	A	6−7
	Co2	375	1.02	35	2	14	B	20−25
	Co3	400	1.02	35	2	13	B	20−25

[a]Two films in sample Co1 were sequentially deposited in different conditions, indicated by order of the appearance of the corresponding value. The precursor solution and resulting film thickness are also indicated.

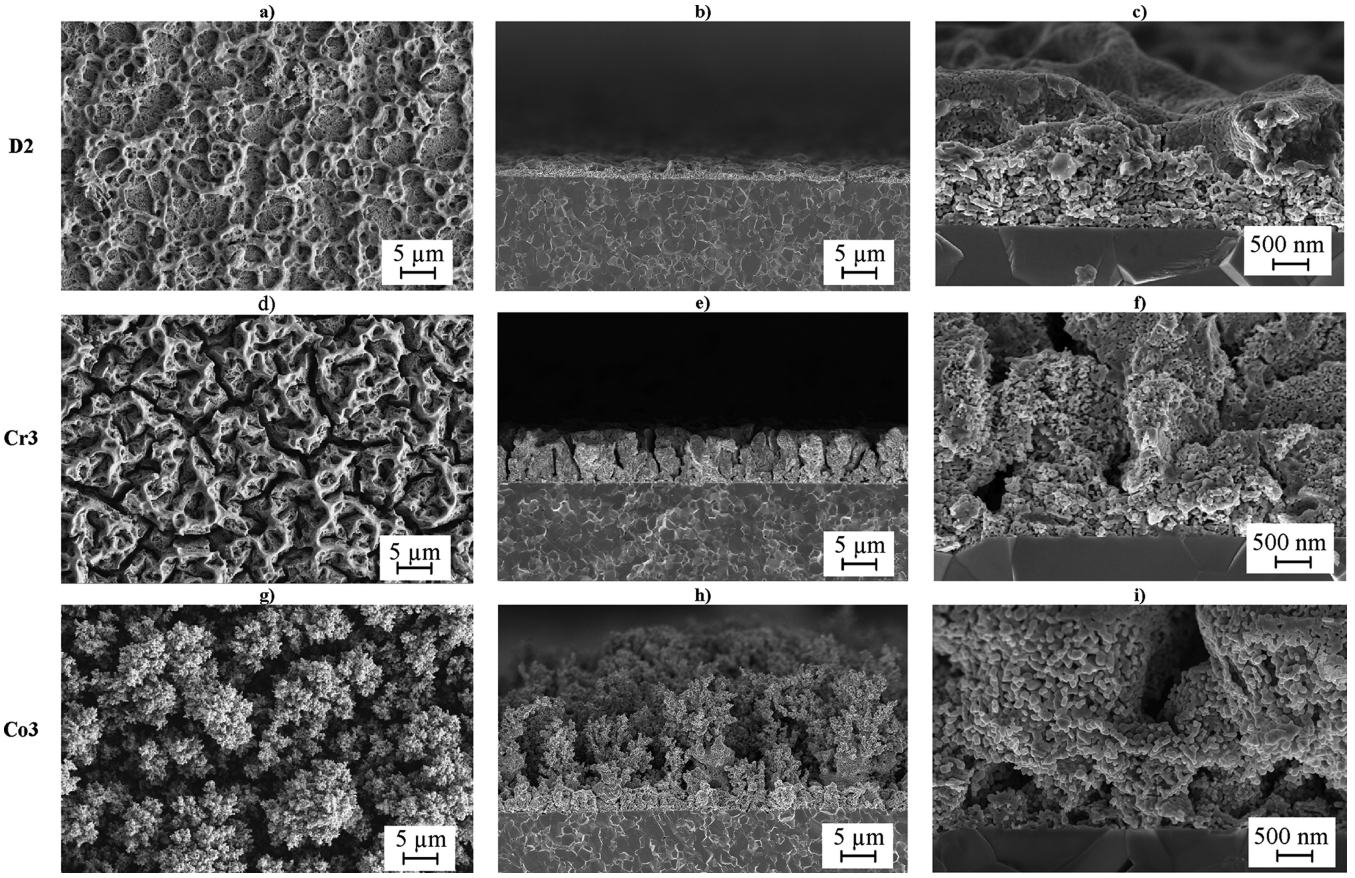

Figure 1. Surface and cross-section SEM micrographs of representative samples types: (a−c) dense, (d−f) cracked and (g−i) coral).

data obtained by focused ion beam−scanning electron beam (FIB-SEM) tomography.

EXPERIMENTAL SECTION

Film Deposition. Several LSCF films with distinct morphologies were deposited on CGO substrates by means of a vertical ESD process.[15] CGO pellets (16−18 mm in diameter and 1.2 − 1.8 mm thick) were prepared from commercial powders (Praxair, 99.9%) calcined at 700 °C for 7 h in air, isostatically pressed at 250 MPa for 5 min and then sintered at 1450 °C for 4 h in air. Both pellet sides were machined with diamond tools and then polished with diamond pastes to guarantee uniform surface conditions before ESD.

A precursor salt solution was prepared by weighing $La(NO_3)_3.6H_2O$ (Prolabo, 99.99%), $SrCl_2.6H_2O$ (Strem Chemicals, 99%), $Co(NO_3)_2.6H_2O$ (Sigma-Aldrich, 99.999%) and $Fe(NO_3)_2.9H_2O$ (Sigma-Aldrich, 99.99%) salts in adequate amounts as to obtain the $La_{0.6}Sr_{0.4}Co_{0.2}Fe_{0.8}O_{3-\delta}$ composition. Two solutions, A and B, were prepared. Solution A was obtained by mixing salts in ethanol (C_2H_5OH, 99.9%; Prolabo) and diethylene glycol monobutyl ether, also known as butyl carbitol ($CH_3(CH_2)_3OCH_2CH_2OCH_2CH_2OH$, 99+%; Acros Organics 99+%) with a 1:2 volume ratio. Solution B was obtained by mixing salts in ethanol and distilled water with a 1:4 volume ratio. A total salt concentration of 0.02 mol L^{-1} was obtained in both solutions.

Depositions were made at nozzle-to-substrate distances, *d*, ranging from 15 to 58 mm, solution flow rates, *Q*, between 0.34 and 1.59 mL h^{-1} using a model A-99, Bioblock Scientific flowmeter. Deposition times, *t*, varied between 1 and 3 h. Substrate temperature varied from 250 to 450 °C with values referring to the surface of the substrate facing the solution spray, obtained after temperature calibration. Positive voltages ranging from 6 to 14 kV were selected and applied between the nozzle and the grounded substrate for aerosol generation

dx.doi.org/10.1021/cm2016998 | *Chem. Mater.* 2011, 23, 5340−5348

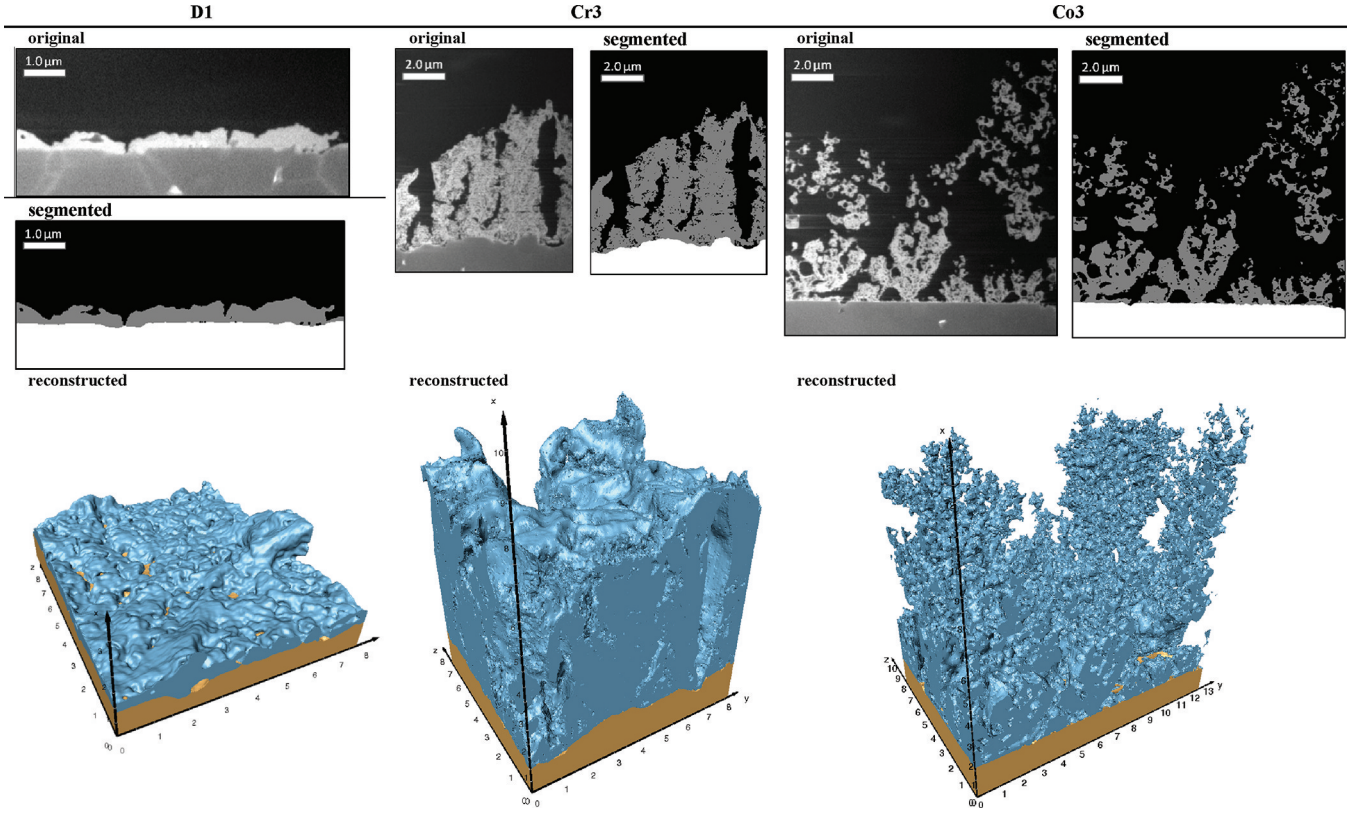

Figure 2. Original FIB-SEM image, segmented image, and final 3D reconstruction of the LSCF cathodes. Blue is LSCF, orange is CGO.

and spray stabilization for each set of parameters. All samples were annealed at 900 °C in air for 2 h. Individual sample preparation conditions are specified in Table 1.

Materials Characterization. FIB-SEM tomography has recently been developed to provide quantitative 3D structural data on SOFC electrodes.[16−23] Initially, imaging was done in a field-emission gun scanning electron microscopy (ZEISS Ultra 55) coupled with an energy dispersive X-ray analyzer (EDX). Fractured cross sections were then vacuum-infiltrated with a low-viscosity resin (Buehler Epothin) and prepared for 3D FIB-SEM tomography. An FEI Helios Nanolab utilizing a 30 kV 0.92 nA ion beam was used to serial section planar slices of the LSCF electrodes. Images were collected using the in-lens detector and 2 kV electron beam energies where 19.2 nm pixel^{-1} x-y resolution and 25 nm pixel^{-1} z resolution was achieved. The volumes measured, ∼1000 μm^3, were large enough to provide good statistics in measuring the micrometer-scale cathode features. Segmentation was carried out using the watershed method as described elsewhere.[24,25] Quantitative analysis of the reconstructed cathodes was completed using in-house code written in Interactive Data Language (IDL).

X-ray powder diffraction was carried out on samples postannealed at 900 °C for 2 h in air using a PANalytical X'Pert Pro MPD diffractometer in the Bragg−Brentano geometry from: 20° to 120° in 2θ (0.017° in 2θ step, 30.5 s as a counting time) with Cu radiation (λ = 0.15418 nm). Crystalline phases were identified using EVA software.

Alternating Current (AC) Impedance Measurements. Impedance measurements were performed on a total of nine samples prepared in a three-electrode configuration, using the LSCF film as working electrode (WE). Platinum paste (Metalor, No. 6982) was painted symmetrically opposite to the WE to serve as the counter electrode (CE). The reference electrode was painted along the circumference of the electrolyte pellet. WE and CE areas were kept constant at ∼0.5 cm^2 and positioned at the center of each side of the CGO pellet. This configuration has been chosen to improve the reliability of impedance measurements since nonsymmetrical arrangement of working and counter electrodes can result in significant errors on both electrolyte and electrode impedances.[26−30] Platinum grids (Heraeus, mesh 3600) mechanically pressed against WE and CE were used as electrical current collectors. Uniaxial pressing was used to flatten platinum grids. Platinum wires (Ögussa, ϕ_{ext} = 0.2 mm) were used to connect all electrodes to the external electric circuit.

Electrochemical characterization was carried out between 400 and 600 °C at open circuit potential (OCP) in ambient air, under atmospheric conditions, using a Solartron (SI 1280B) potentiostat/galvanostat frequency response analyzer with frequencies ranging between 0.01 Hz and 20 kHz at 13 steps per decade. The amplitude of the measuring sinusoidal voltage equal to 10 mV was chosen to ensure the linearity of the electrical response. The numbers on impedance diagrams indicate the logarithm of the measuring frequency. All impedance diagrams have been normalized to the WE area. Impedance diagrams were fitted to equivalent circuits using the ZView software (Scribner Associates).

RESULTS AND DISCUSSION

Microstructures. The microstructure of films deposited by ESD is mainly determined by the size of the droplets that form the aerosol. For a fixed precursor solution the droplet size decreases with increasing substrate temperature and nozzle-to-substrate distance, and increases with solution flow rate.[15] In this work the deposition conditions were selected accordingly (Table 1) in preparing a total of nine samples, grouped according to the external surface of the cathode microstructures. These are henceforth referred to as dense (Figure 1a-c), cracked (Figure 1d−f) and coral (Figure 1g−i) and abbreviated to D, Cr and Co, respectively. In each set of microstructures the thickness of the films was varied. Depending on the type of microstructure, increasing deposition time may cause microstructural variation in the films. Consequently, to maintain the general microstructure it is sometimes necessary to adjust other deposition parameters. Images collected during FIB-SEM serial sectioning and

dx.doi.org/10.1021/cm2016998 | Chem. Mater. 2011, 23, 5340−5348

corresponding segmented images, along with 3D reconstructions, are shown in Figure 2. It is interesting to note that two different length scales exist in the cracked and coral microstructures. The macro structure is on the order of micrometers, but the internal porosity is smaller than 100 nm. It is possible that pores smaller than ~20 nm were present but were not resolved by the FIB-SEM, such that the measured LSCF interfacial areas may be underestimated.

The so-called dense cathodes feature thicknesses ranging from 1 to 4 μm and maximum variations of ~1 μm due to superficial film roughness. Adequate film-to-substrate adhesion was verified by a scotch-tape test. The LSCF-pore interfacial area, measured from the 3D images and normalized by the electrode geometrical area, was found to be 2.0.

The microstructural type referred to as cracked exhibits film thickness varying between 3 and 8 μm consisting of noncontinuous reticulated surfaces, with ~1 μm gaps visible throughout the surface. This type of morphology is obtained when liquid content in the droplets is high, so that stresses generated by drying and contraction of the film during subsequent heat treatment yield severe cracking. The electrode−pore interfacial area, normalized to the geometrical area, was 24.7, a substantial increase relative to the dense sample. The larger surface area was not only a result of the macrocracking in the film, but also due to fine internal pore structure not observed in the dense electrode.

The coral microstructures have very distinct features, with solid particles arranged in highly ramified structures, and thickness up to 25 μm. These structures are formed when the size of the airborne droplets is very small and surface charge causes them to be attracted toward specific areas of the film, in what is called the preferential landing effect.[14] The substitution of butyl-carbitol in solution A, by water in solution B, decreases the evaporation temperature by ~100 °C, allowing the droplets to dry quicker. To enhance the preferential landing effect, solution B was used in preparing samples Co2 and Co3. In these samples, the intermediate layer is ~2 μm thick. Normalized interfacial electrode-pore area was 28.2, similar to the cracked structure. However, and contrarily to the cracked structure, the largest contribution to the interfacial area in coral samples originates from the fine outer structure of the film.

Film elemental composition was accessed by EDX analysis. Semiquantitative results of representative samples (Table 2)

Table 2. Chemical Composition of LSCF Films Determined by Semi-Quantitative EDX Analysis, In Atomic Percentage

	chemical composition (at %)			
sample	La	Sr	Co	Fe
D1	59	41	23	77
Cr3	59	41	19	81
Co2	62	38	21	79
Co3	72	28	21	79

show that the Co/Fe ratios match the values expected for the $La_{0.6}Sr_{0.4}Co_{0.2}Fe_{0.8}O_{3-\delta}$ composition. A slight variation in the La/Sr ratio was observed in sample Co3. As this sample was prepared using the same precursor solution as in sample Co2 (Solution B), variation is most probably due to different EDX analysis conditions, e.g., interaction volume and shadow effects.

XRD was done on postannealed samples before and after the impedance spectroscopy analysis. Representative patterns obtained before and after electrical measurements (Figure 3)

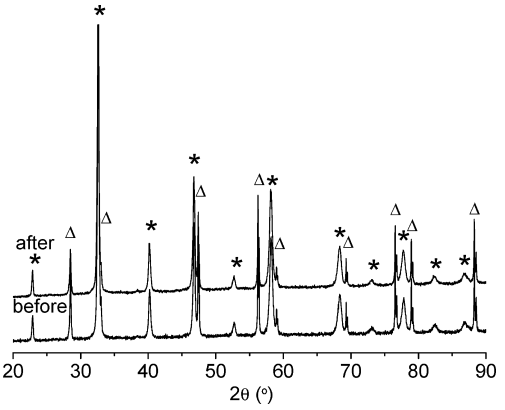

Figure 3. XRD patterns obtained for sample Cr3 before and after the impedance spectroscopy analysis. Peaks corresponding to the LSCF and CGO phases are identified by * and Δ symbols, respectively.

show two crystalline phases, corresponding to the LSCF perovskite film and CGO from the substrate. No secondary phases and no peak-shift were observed, consistent with a stoichiometric perovskite LSCF phase and indicating no phase reactivity occurred during platinum annealing or electrochemical testing. Crystallite sizes of LSCF films deposited by ESD have been previously determined to range between 28 and 46 nm,[31] matching well with the microstructural imaging analysis in this study.

AC Impedance. Impedance diagrams recorded in air at OCP in the vicinity of 500 °C for all investigated films are shown in Figure 4. The high frequency intercepts were set to zero in order to provide a clear comparison between the polarization arcs. Note that there was some sample-to-sample variation in the high frequency intercept, which is nominally associated with the electrolyte ohmic resistance, but the polarization arcs were nevertheless quite consistent. Their shape is similar to those recorded on LSCF-based electrodes in the same temperature range.[32−36] The total polarization resistance, $R_{pol,}$ is defined by the difference between the intersections of low and high frequency limits of the electrode impedance with the real axis in the Nyquist plane. For LSCF films with thicknesses ranging from 0.2 to 30 μm, $R_{pol,}$ is reported to vary between 0.5 and 122 Ω cm^2 at 600 °C in air.[6,32,37−42] In this regard, it is worth noting that the polarization resistance of sample Co1 (0.82 Ω cm^2) is among the lowest reported in the literature at 600 °C. This indicates that nanostructured MIEC electrodes can be regarded as promising candidates for cathodes at intermediate temperatures.

Figure 5 shows Arrhenius plot of R_{pol} for all electrodes. The values of activation energy, $E_{a,}$ determined from the linear dependence versus the reciprocal temperature are arranged in Table 3.

E_a values (Table 3) are comparable to those reported in the literature for LSCF-based cathodes of similar compositions contacted with CGO electrolytes in air, ranging from 1.23 to 1.69 eV for temperatures up to 800 °C.[35,37−41,43,44] Among them, the value reported by Hsu and Hwang[40] for $La_{0.6}Sr_{0.4}Co_{0.2}Fe_{0.8}O_{3-\delta}$ cathodes prepared by ultrasonic spray pyrolysis and with a microstructure close to that of cracked samples (1.23 eV) is closer to our findings. In agreement with previous reports,[32,45] these values fall between the activation energy of the surface exchange coefficient and that of the tracer diffusion coefficient.

dx.doi.org/10.1021/cm2016998 | Chem. Mater. 2011, 23, 5340−5348

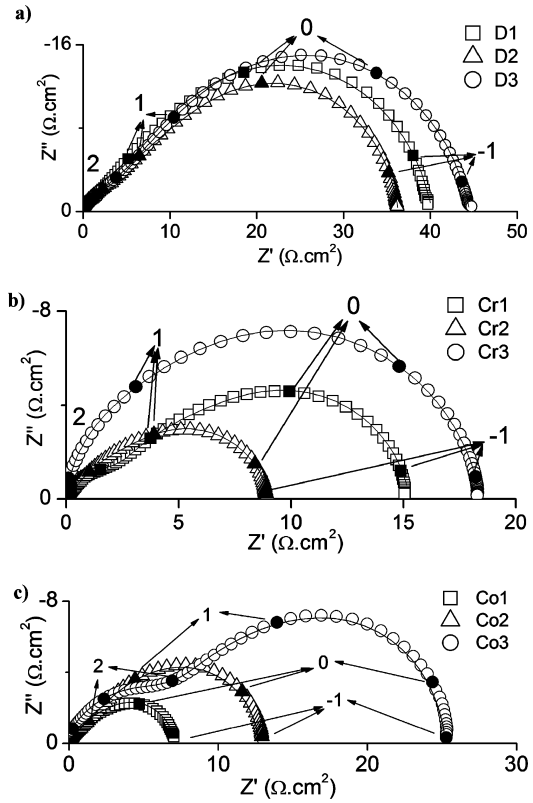

Figure 4. Nyquist plots for (a) dense, (b) cracked, and (c) coral samples at ~500 °C (normalized values). Line plots correspond to the fitting result. Numbers above plots indicate the logarithm of the measuring frequency.

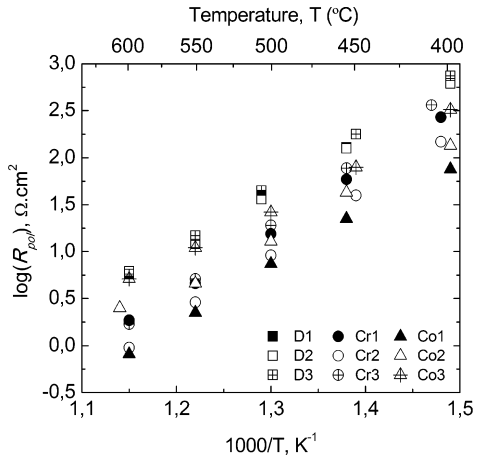

Figure 5. Arrhenius plots of the polarization resistance, R_{pol}, for all samples.

To the best of our knowledge, impedance diagrams of LSCF-based electrodes are typically composed of two or three elementary contributions, depending on electrode microstructure, composition and temperature range. In the present study, the experimental impedance plots were fitted according to the equivalent circuit shown in Figure 6, where R1, W1 and R2 elements correspond respectively to the high-frequency, HF, medium-frequency, MF, and low-frequency, LF, features. Previous works have argued for similar models for oxygen reduction on MIEC electrodes.[46,47] The constant phase elements, CPE, added to the HF and LF features replace

Table 3. Activation Energies, E_a, for R_{pol} and the High-, Medium-, and Low-Frequency (HF, MF, and LF, respectively) Contributions

		E_a (eV)			
microstructure	sample	HF	MF	LF	R_{pol}
dense	D1	0.15	1.14	1.29	1.18
	D2	0.41	1.17	1.31	1.18
	D3	0.92	0.80	1.34	1.24
cracked	Cr1	0.69	1.22	1.42	1.28
	Cr2		1.13	1.32	1.30
	Cr3		1.13	1.44	1.46
coral	Co1		0.90	1.29	1.15
	Co2	0.60	1.11	1.05	1.03
	Co3	0.64	0.85	1.31	1.05

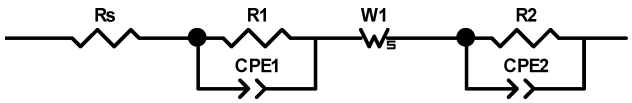

Figure 6. Equivalent circuit model used for impedance spectra fitting.

pure capacitances to appropriately describe the nonideal behavior of impedance semicircles depressed below the real axis in the Nyquist plane. The impedance of a CPE element is given by $Z = (Q(iw)^n)^{-1}$ where Q and n are the fitting parameters and w the angular frequency. The value of the related capacitance, C, was calculated according to $C = (R^{1-n}Q)^{1/n}$.

The three elementary impedance responses (HF, MF, and LF) are common to all investigated electrodes. The evolution of the corresponding apex frequencies as a function of the reciprocal temperature shows well-limited frequency domains within which common responses are grouped (Figure 7).

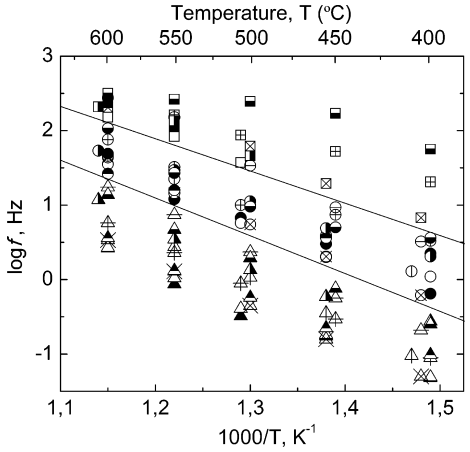

Figure 7. Apex frequencies of the individual cathode responses versus the reciprocal temperature, with HF (square symbols), MF (round symbols), and LF (triangle symbols). The solid lines delimit the frequency domains typical of each phenomena.

The HF contribution of the polarization resistance is shown in Figure 8. In the chosen experimental conditions, the HF feature of the electrode characteristic was not always well-defined, being either incomplete at lower temperatures or deformed by inductive effects from the measurement rig at higher temperatures. Although some scattering of the corresponding electrical parameters was noted, enough

dx.doi.org/10.1021/cm2016998 | Chem. Mater. 2011, 23, 5340–5348

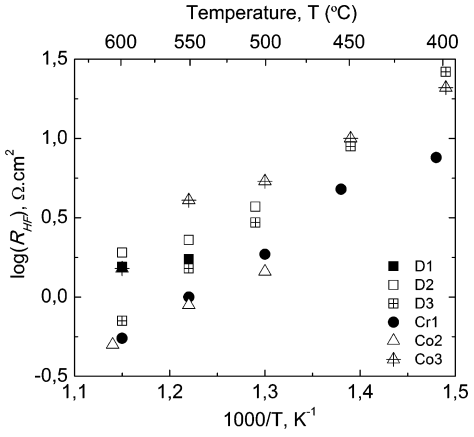

Figure 8. Arrhenius plots of the resistance associated with the high-frequency response, R_{HF}.

information was still present to quantify activation energies for this feature.

Values for E_a, ranged from 0.15 to 0.92 eV (Table 3) with the majority found lower than 0.7 eV. Regardless the origin of the described step, they are lower than those reported in the literature for LSCF-based films by Baumann et al. (1.55 eV)[48] and Xiong et al. (1.34 eV).[49] Nonetheless, in similar - but dense - LSCF electrodes, detailed impedance spectroscopy of the HF feature suggested a relation to oxygen transfer across the LSCF/CGO interface,[50] as has been observed elsewhere.[49,51−53]

The capacitance associated to the HF contribution is nearly independent of the measuring temperature (Figure 9),

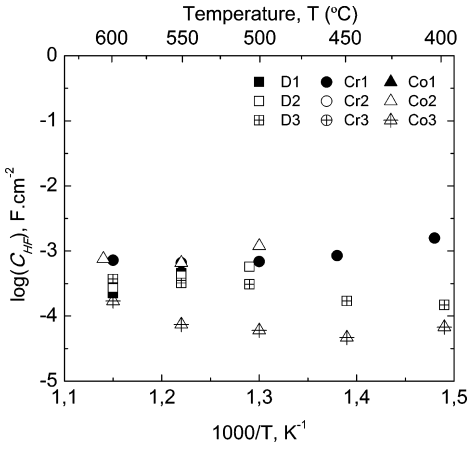

Figure 9. Capacitance values of the high-frequency response, C_{HF}, versus the reciprocal temperature.

consistent with the behavior of an interfacial capacitance coupled to a charge transfer process.[54] Between 400 and 600 °C, the average C_{HF} value is around 4×10^{-4} F cm^{-2}, with maximum and minimum values determined for samples Cr1 (1.5×10^{-3} F.cm^{-2}) and Co1 (5×10^{-5} F cm^{-2}), respectively. These values are similar to those measured for the ionic transfer process reported by Baumann et al.[48] on thin, dense LSCF electrodes where C_{HF} at 500 °C was observed to be 9×10^{-5} and 6×10^{-4} F cm^{-2} upon changing from YSZ to CGO/YSZ electrolytes. These general similarities suggest that the HF feature measured herein is related to the interfacial LSCF-GDC charge transfer.

Alternatively, other studies show no evidence for the contribution of the electrode/electrolyte interface,[47,52] agreeing with assumptions that this charge transfer is facile.[52] However, in thick LSCF-based electrodes[47] one can expect a strong overlapping between the corresponding small interfacial contribution and the increasing impedance response due to ionic diffusion in the electrode material,[35,47] particularly if denser electrodes are used. The assignment of the HF response to the ionic charge transfer process at the electrode/electrolyte interface[49−53] is furthermore corroborated by the variation of the equilibrium electrode impedance as a function of the nature of the electrolyte material.[44,48,55,56]

According to the equivalent circuit chosen in this study, the impedance contribution in the medium frequency range, MF, was described by a Warburg-type impedance which can be related to the oxygen vacancy diffusion through the electrode material.[35,37,39,45,56,57] For porous $La_{0.6}Sr_{0.4}Co_{0.8}Fe_{0.2}O_{3-\delta}$ electrodes contacted with CGO, experimental impedance diagrams were analyzed according to a Gerischer- or a Warburg-type impedance and the best fit was reached by using the latter.[46] It is worth mentioning that the prevalence of a Warburg-type impedance does not necessarily mean that bulk diffusion is the only rate-determining step corresponding to the related impedance contribution.[58,59] It simply indicates that the overall reaction mechanism involves a diffusion step.

The expression of the Warburg impedance[60] is given by

$$Z_w(w) = \frac{RT}{4F^2}\frac{1}{SC_0}\frac{th(l\sqrt{jw/D_v})}{\sqrt{jw/D_v}} \quad (1)$$

where R and F are the gas and Faraday constants, respectively, S the electrode/electrolyte interface area, C_0 the oxygen vacancy concentration in equilibrium with air, D_v the oxygen vacancy diffusion coefficient and ω the angular frequency. The parameter l corresponds to the effective length wherein the electrode is electrochemically active. In case of a dense electrode, l corresponds to the total electrode thickness whereas for porous electrodes it is expected to be lower.[48,59,61,62] Contrary to other studies,[63,64] no significant correlation between R_{MF} and film thickness was observed, despite thickness variations of an order of magnitude (Table 1 and Figure 10), suggesting that only a fraction of the electrode is electrochemically active.[10−12,65]

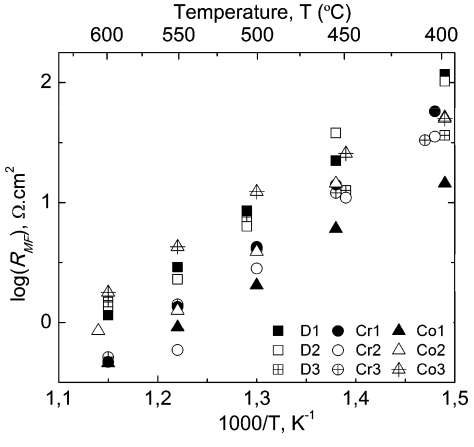

Figure 10. Arrhenius plots of the resistance associated with the medium-frequency response, R_{MF}.

dx.doi.org/10.1021/cm2016998 | Chem. Mater. 2011, 23, 5340−5348

For all investigated films, the apex frequency of the Warburg-type impedance varies between 0.6 and 250 Hz for temperatures ranging from 400 to 600 °C (Figure 7). At 500 °C in air, the value of the apex frequency of the impedance loop related to bulk diffusion in dense cathodes is around 6 Hz, similar to values for 0.35 μm dense $La_{0.7}Sr_{0.3}CoO_{3-\delta}$ films reported elsewhere.[63] Between 400 and 600 °C, the activation ranges from 0.80 to 1.17 eV, averaging 1.05 eV. Regardless of electrode morphology, no significant variation of the E_a values as a function of the film thickness can be deduced (Table 3 and Figure 10) indicating that the related diffusion process within the active length is identical for all electrodes. These values are lower than previously published data on LSCF-based cathodes with different dopant contents.[35,46,66] However, similar values have been reported for a $La_{0.1}Sr_{0.9}Co_{0.8}Fe_{0.2}O_{3-\delta}$ porous cathode[46] and a thin dense $La_{0.7}Sr_{0.3}CoO_{3-\delta}$ film,[63] with E_a values for Warburg resistance found equal to 1.0 and 1.08 eV, respectively. The preceding analysis therefore suggests the assignment of the MF contribution to finite length diffusion is reasonable.

Within experimental accuracy, the apex frequencies related to *LF* contribution in the electrode characteristics are comparable in all samples (Figure 7), indicating that the described process remains similar versus the electrode microstructure. The associated resistance, R_{LF}, is the largest contribution to R_{pol} in all cathodes (Figure 4) and especially at low temperatures, in agreement with previous studies.[36,67] As shown in Figure 11,

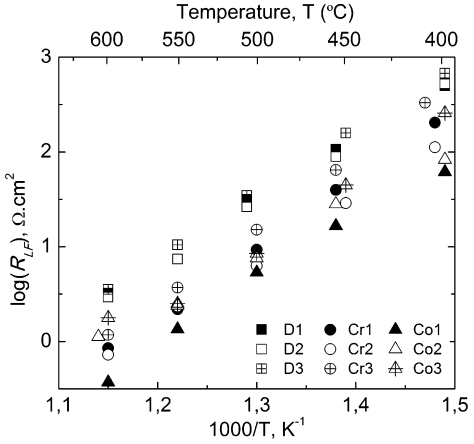

Figure 11. Arrhenius plots of the resistance associated with the low-frequency response, R_{LF}.

the most developed surface areas in cracked and coral cathodes yield lower R_{LF} values and thus lower R_{pol} values, relative to dense samples.

Between 400 and 600 °C, the activation energy of the *LF* contribution varies between 1.05 and 1.44 eV (Table 3). These values match well with previously published results in spite of different morphologies and/or compositions. Indeed, values ranging from 1.1 to 1.6 eV were determined for thin dense films of similar composition[49,68] and the activation energy was found to vary between 1.42 and 1.47 eV for porous LSC as a function of the La/Sr ratio.[69] The present *LF* response is clearly not concentration polarization (either gas diffusion or gas conversion), since these are not thermally activated processes.[70,71] The *LF* response can be attributed to oxygen surface exchange reaction,[43] as already suggested for LSCF based cathodes.[4,32,38,44,46,61,66,72] A further argument in favor of this assignment is based on the corresponding capacitance values, C_{LF} (Figure 12). In the chosen experimental conditions, C_{LF}

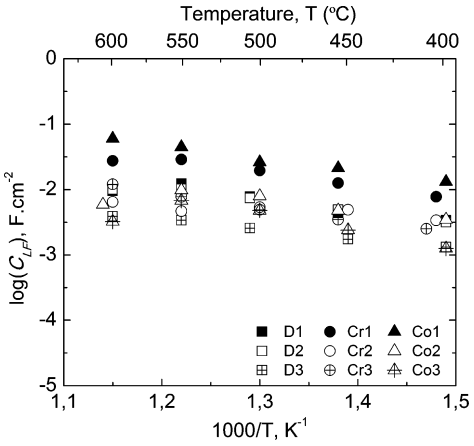

Figure 12. Capacitance values of the low-frequency response, C_{LF}, versus the reciprocal temperature.

typically varies between 1.3 mF.cm^{-2} (sample D3) and 60 mF.cm^{-2} (sample Co1). Regardless of the electrode morphology, C_{LF} increases slightly with temperature, as already observed in porous $La_{1-x}Sr_xCo_{1-y}Ni_yO_{3-\delta}$ cathodes.[73] From an electrical standpoint, this capacitive process can be related to a chemical capacitance taking into account the change of the oxygen content in the electrode material and it is thus proportional to the volume of the electrode.[74,75]

Since the equivalent circuit analysis clearly indicates that the electrode reaction is dominated by solid state diffusion and surface exchange phenomena, the Adler-Lane-Steele (ALS) model[65] was used to predict the impedance response and polarization resistance based on material and microstructural parameters for representative samples D1, Cr3 and Co3. In this approach the Warburg and *R//CPE* elements used in the equivalent circuit at, respectively, medium and low frequencies, are replaced by a Gerischer element that models the combined impedance response. This response is described by eq 2 where R_{chem} is a characteristic resistance, and t_{chem} is a characteristic time constant. The polarization resistance is modeled by a mix of material and microstructural parameters (eq 3). Values of a and ε were obtained from the 3D reconstructions of the electrodes while values for D^* and k were obtained from Benson[76] and found to be, respectively, 5.6×10^{-12} cm^2.s^{-1} and 2.16×10^{-8} cm.s^{-1} at 500 °C. Resulting values are compared with the resistance obtained from the sum of *MF* and *LF* circuit element fits at that temperature for verification.

$$Z_w = R_{chem}\left(\sqrt{\frac{1}{1 - jwt_{chem}}}\right) \quad (2)$$

$$R_{pol} = \frac{RT}{2F^2}\left(\sqrt{\frac{\tau}{(1-\varepsilon)aD^*kC_0^2}}\right) \quad (3)$$

The multiple pore length scales of the present structures do not match directly with the homogeneous pore structure assumed in the ALS model, and hence the present predictions must be considered approximate. The smaller scale "internal porosity" was used for ε in the calculations since it was more prevalent in the electrochemically active region near the electrolyte. The ε

dx.doi.org/10.1021/cm2016998 | *Chem. Mater.* 2011, 23, 5340–5348

values, obtained by eroding away internal pores and comparing with the original structure, were 8.95, 6.75, and 11.1 vol % for the D, Cr, and Co microstructures. The pore-electrode interfacial area, a, was calculated by meshing the voxelized electrode structure and normalizing by the LSCF electrode volume. Values of 4.70, 8.63, and 15.9 μm^{-1} were calculated for the D1, Cr3, and Co3 structures. Interfacial areas were larger for the cracked and coral structures, and are likely even higher since pores smaller than the FIB-SEM resolution limit (~20 nm) were not properly resolved. This is more likely a factor for the cracked structure, which presents very large amounts of internal nanoscale porosity. Tortuosity values were not measured and assumed, for simplicity, to be unity; in any case, the results were not strongly dependent on the tortuosity value. Finally the oxygen concentration, C_0, in the cathode was approximated as 0.084 using a lattice constant of 3.9 Å at 500 °C as measured by Mizusaki for this LSCF composition.[77]

Polarization resistance values of 57, 42, and 31 Ω cm^2 for the D1, Cr3, and Co3 structures were calculated for 500 °C using the above inputs in the ALS model. These values are in reasonable agreement with value trend corresponding to the sum of R_{MF} and R_{LF} elements from the equivalent circuit fitting analysis, of 40, 19.3, and 20.5 Ω cm^2 for the same samples.

The electrochemically active penetration depth of the LSCF electrode was also calculated with the ALS model according to eq Eq. 4. The penetration depth is found to be 710, 530, and 380 nm at 500 °C for the dense, cracked and coral structures, respectively. Even at higher testing temperatures of 600 °C with D^* and k equal to 1.74×10^{-10} and 1.26×10^{-7} cm s^{-1}, the penetration depth remained below 1.6 μm. This confirms earlier observations that R_{MF} element resistance did not change with increasing electrode thickness.

$$\delta = \sqrt{\frac{(1-\varepsilon)D^*}{\tau a k}} \qquad \text{(Eq. 4)}$$

Electrode-pore surface area is clearly responsible for the difference in electrode polarization resistance observed in the model. This compares nicely with the observed realization that the dense structures had the highest R_{pol} values, while the cracked and coral structures were observed to have the best overall performance (Figure 11). The polarization resistance predicted based on microstructural data was generally higher than experimentally measured, a discrepancy that might be explained by underestimation of the pore-electrode surface area due to the 20 nm resolution limit of the FIB-SEM. Another possible source of error is that the ALS model assumes that the electrode is a homogeneous structure, though it is clearly not for the cracked and coral samples. Overall, however, the model predicts the polarization resistance within a factor of 2, reasonable results given that no fitting parameters were employed.

CONCLUSIONS

In this work, the oxygen reduction on mixed conducting $La_{0.6}Sr_{0.4}Co_{0.2}Fe_{0.8}O_{3-\delta}$ electrodes with various microstructures obtained by ESD has been investigated using impedance spectroscopy. A detailed microstructural characterization was obtained using 3D FIB-SEM tomography. The electrode characteristics exhibited similar patterns with respect to temperature in air. Up to three elementary steps have been identified by equivalent circuit fitting at decreasing measuring frequencies: charge transfer process at the LSCF/CGO interface, a diffusion process within the volume of LSCF, and oxygen transfer at the LSCF/gas interface. Comparison of FIB-SEM 3D microstructural analysis with electrochemical measurements confirms that larger cathode surface areas yield better electrochemical performances. The Adler-Lane-Steele model combined with measured microstructural data provided a good prediction of the observed performance trend in samples with different surface areas. It also suggested that the electrochemically active penetration depth was no greater than 1.6 μm from the electrolyte − in agreement with the lack of relationship between the MF element resistance and electrode thickness. This study has confirmed that the rate-limiting step in LSCF electrodes is surface exchange, regardless of the considerable morphological and thickness differences in the investigated films.

AUTHOR INFORMATION

Corresponding Author

*Tel: +33-4-7682-6684. Fax: +33-4-7682-6777. E-mail: elisabeth.djurado@lepmi.grenoble-inp.fr.

REFERENCES

(1) Tai, L. W.; Nasrallah, M. M.; Anderson, H. U.; Sparlin, D. M.; Sehlin, S. R. *Solid State Ionics* **1995**, *76*, 259−271.
(2) Tai, L. W.; Nasrallah, M. M.; Anderson, H. U.; Sparlin, D. M.; Sehlin, S. R. *Solid State Ionics* **1995**, *76*, 273−283.
(3) Tsipis, E. V.; Kharton, V. V. *J. Solid State Electrochem.* **2008**, *12*, 1039−1060.
(4) Kan, C. C.; Kan, H. H.; Van Assche, F. M.; Armstrong, E. N.; Wachsman, E. D. *J. Electrochem. Soc.* **2008**, *155*, B985−B993.
(5) Xie, Y. S.; Neagu, R.; Hsu, C. S.; Zhang, X. G.; Deces-Petit, C.; Qu, W.; Hui, R.; Yick, S.; Robertson, M.; Maric, R.; Ghosh, D. *J. Fuel Cell Sci. Technol.* **2010**, *7*, 021007−6.
(6) Lee, J. W.; Liu, Z.; Yang, L.; Abernathy, H.; Choi, S. H.; Kim, H. E.; Liu, M. L. *J Power Sources* **2009**, *190*, 307−310.
(7) Beckel, D.; Bieberle-Hutter, A.; Harvey, A.; Infortuna, A.; Muecke, U. P.; Prestat, M.; Rupp, J. L. M.; Gauckler, L. J. *J. Power Sources* **2007**, *173*, 325−345.
(8) Baque, L.; Serquis, A. *Appl. Surf. Sci.* **2007**, *254*, 213−218.
(9) Baque, L.; Caneiro, A.; Moreno, M. S.; Serquis, A. *Electrochem. Commun.* **2008**, *10*, 1905−1908.
(10) Peters, C.; Weber, A.; Ivers-Tiffée, E. *J. Electrochem. Soc.* **2008**, *155*, B730−B737.
(11) Marinha, D.; Hayd, J.; Dessemond, L.; Ivers-Tiffée, E.; Djurado, E. *J. Power Sources* **2011**, *196*, 5084−5090.
(12) Adler, S. B. *Chem. Rev.* **2004**, *104*, 4791−4843.
(13) Gañan-Calvo, A. M.; Davila, J.; Barrero, A. *J. Aerosol Sci.* **1997**, *28*, 249−275.
(14) Chen, C. H.; Kelder, E. M.; vanderPut, P. J. J. M.; Schoonman, J. *J. Mater. Chem.* **1996**, *6*, 765−771.
(15) Marinha, D.; Rossignol, C.; Djurado, E. *J. Solid State Chem.* **2009**, *182*, 1742−1748.
(16) Wilson, J. R.; Kobsiriphat, W.; Mendoza, R.; Chen, H.-Y.; Hiller, J. M.; Miller, D. J.; Thornton, K.; Voorhees, P. W.; Adler, S. B.; Barnett, S. A. *Nat. Mater.* **2006**, *5*, 541−544.
(17) Iwai, H.; Shikazono, N.; Matsui, T.; Teshima, H.; Kishimoto, M.; Kishida, R.; Hayashi, D.; Matsuzaki, K.; Kanno, D.; Saito, M.; Muroyama, H.; Eguchi, K.; Kasagi, N.; Yoshida, H. *J. Power Sources* **2009**, *195*, 955−961.
(18) Gostovic, D.; Smith, J. R.; Kundinger, D. P.; Jones, K. S.; Wachsman, E. D. *Electrochem. Solid-State Lett.* **2007**, *10*, B214−B217.
(19) Jørgensen, P. S.; Hansen, K. V.; Larsen, R.; Bowen, J. R. *Ultramicroscopy* **2010**, *110*, 216−228.
(20) Wilson, J. R.; Cronin, J. S.; Barnett, S. A. *Scr. Mater.* **2010**, *65*, 67−72.

(21) Wilson, J. R.; Cronin, J. S.; Duong, A. T.; Rukes, S.; Chen, H.-Y.; Thornton, K.; Mumm, D. R.; Barnett, S. *J. Power Sources* **2009**, *195*, 1829−1840.
(22) Shikazono, N.; Kanno, D.; Matsuzaki, K.; Teshima, H.; Sumino, S.; Kasagi, N. *J. Electrochem. Soc.* **2010**, *157*, B665−B672.
(23) Shearing, P. R.; Cai, Q.; Golbert, J. I.; Yufit, V.; Adjiman, C. S.; Brandon, N. P. *J. Power Sources* **2010**, *195*, 4804−4810.
(24) Roerdink, J. B. T. M.; Meijster, A. *Fundamenta Informaticae* **2000**, *41*, 187−228.
(25) Gulsoy, E. B. *Computational Tools for Automated Analysis of Three-Dimensional Microstructural Characterization Data*; Carnegie Mellon University: Pittsburgh, PA, 2010.
(26) Nagata, M.; Itoh, Y.; Iwahara, H. *Solid State Ionics* **1994**, *67*, 215−224.
(27) Jiang, Y.; Virkar, A. V.; Zhao, F. *J. Electrochem. Soc.* **2001**, *148*, A1091−A1099.
(28) Hsieh, G.; Ford, S. J.; Mason, T. O.; Pederson, L. R. *Solid State Ionics* **1996**, *91*, 191−201.
(29) Hsieh, G.; Mason, T. O.; Garboczi, E. J.; Pederson, L. R. *Solid State Ionics* **1997**, *96*, 153−172.
(30) Kato, T.; Momma, A.; Kaga, Y.; Nagata, S.; Kasuga, Y.; Kitase, M. *Solid State Ionics* **2000**, *132*, 287−295.
(31) Marinha, D.; Djurado, E. *ECS Meet. Abstr.* **2010**, *1001*, 708−708.
(32) Esquirol, A.; Brandon, N. P.; Kilner, J. A.; Mogensen, M. *J. Electrochem. Soc.* **2004**, *151*, A1847−A1855.
(33) Jiang, S. P. *Solid State Ionics* **2002**, *146*, 1−22.
(34) Liu, J. B.; Co, A. C.; Paulson, S.; Birss, V. I. *Solid State Ionics* **2006**, *177*, 377−387.
(35) Kournoutis, V. C.; Tietz, F.; Bebelis, S. *Fuel Cells* **2009**, *9*, 852−860.
(36) Shah, M.; Barnett, S. A. *Solid State Ionics* **2008**, *179*, 2059−2064.
(37) Leng, Y. J.; Chan, S. H.; Liu, Q. L. *Int. J. Hydrogen Energy* **2008**, *33*, 3808−3817.
(38) Lou, X. Y.; Wang, S. Z.; Liu, Z.; Yang, L.; Liu, M. L. *Solid State Ionics* **2009**, *180*, 1285−1289.
(39) Hwang, H. J.; Ji-Woong, M. B.; Seunghun, L. A.; Lee, E. A. *J. Power Sources* **2005**, *145*, 243−248.
(40) Hsu, C. S.; Hwang, B. H. *J. Electrochem. Soc.* **2006**, *153*, A1478−A1483.
(41) Beckel, D.; Muecke, U. P.; Gyger, T.; Florey, G.; Infortuna, A.; Gauckler, L. J. *Solid State Ionics* **2007**, *178*, 407−415.
(42) Bae, J. M.; Steele, B. C. H. *Solid State Ionics* **1998**, *106*, 247−253.
(43) Murray, E. P.; Sever, M. J.; Barnett, S. A. *Solid State Ionics* **2002**, *148*, 27−34.
(44) Zhou, W. I.; Shao, Z. P.; Ran, R.; Gu, H. X.; Jin, W. Q.; Xu, N. P. *J. Am. Ceram. Soc.* **2008**, *91*, 1155−1162.
(45) Leonide, A.; Ruger, B.; Weber, A.; Meulenberg, W. A.; Ivers-Tiffée, E. *J. Electrochem. Soc.* **2010**, *157*, B234−B239.
(46) Grunbaum, N.; Dessemond, L.; Fouletier, J.; Prado, F.; Caneiro, A. *Solid State Ionics* **2006**, *177*, 907−913.
(47) Kim, Y. M.; Pyun, S. I.; Kim, J. S.; Lee, G. J. *J. Electrochem. Soc.* **2007**, *154*, B802−B809.
(48) Baumann, F. S.; Fleig, J.; Habermeier, H. U.; Maier, J. *Solid State Ionics* **2006**, *177*, 1071−1081.
(49) Xiong, H.; Lai, B. K.; Johnson, A. C.; Ramanathan, S. *J Power Sources* **2009**, *193*, 589−592.
(50) Lynch, M. E.; Mebane, D. S.; Liu, Y. J.; Liua, M. L. *J. Electrochem. Soc.* **2008**, *155*, B635−B643.
(51) Liu, S. M.; Suo, J. P.; Xiao, J. Z. *Int. J. Hydrogen Energy* **2008**, *33*, 6322−6326.
(52) Prestat, M.; Infortuna, A.; Korrodi, S.; Rey-Mermet, S.; Muralt, P.; Gauckler, L. J. *J. Electroceram.* **2007**, *18*, 111−120.
(53) Murray, E. P.; Tsai, T.; Barnett, S. A. *Solid State Ionics* **1998**, *110*, 235−243.
(54) Jiang, S. P.; Wang, W.; Zhen, Y. D. *J. Power Sources* **2005**, *147*, 1−7.
(55) Liu, M. L.; Wu, Z. L. *Solid State Ionics* **1998**, *107*, 105−110.
(56) Lee, S.; Song, H. S.; Hyun, S. H.; Kim, J.; Moon, J. *J. Power Sources* **2009**, *187*, 74−79.
(57) Jiang, S. P.; Love, J. G.; Apateanu, L. *Solid State Ionics* **2003**, *160*, 15−26.
(58) Deseure, J.; Bultel, Y.; Dessemond, L.; Siebert, E. *Solid State Ionics* **2005**, *176*, 235−244.
(59) Adler, S. B. *Solid State Ionics* **1998**, *111*, 125−134.
(60) Raistrick, I. D.; Macdonald, J. R.; Franceschetti, D. R. *Impedance Spectroscopy: Emphasizing Solid Materials and Systems*; John Wiley and Sons: New York, 1987.
(61) Bouwmeester, H. J. M.; Kruidhof, H.; Burggraaf, A. J. *Solid State Ionics* **1994**, *72*, 185−194.
(62) Steele, B. C. H. *Solid State Ionics Solid State Ionics* **1995**, *75*, 157−165.
(63) Ringuedé, A.; Guindet, J. *Ionics* **1997**, *3*, 256−260.
(64) Prestat, M.; Koenig, J. F.; Gauckler, L. J. *J. Electroceram.* **2007**, *18*, 87−101.
(65) Adler, S. B.; Lane, J. A.; Steele, B. C. H. *J. Electrochem. Soc.* **1996**, *143*, 3554−3564.
(66) Esquirol, A.; Kilner, J.; Brandon, N. *Solid State Ionics* **2004**, *175*, 63−67.
(67) Hansen, K. K.; Hansen, K. V. *Solid State Ionics* **2007**, *178*, 1379−1384.
(68) Baumann, F. S.; Fleig, J.; Cristiani, G.; Stuhlhofer, B.; Habermeier, H. U.; Maier, J. *J. Electrochem. Soc.* **2007**, *154*, B931−B941.
(69) Horita, T.; Yamaji, K.; Sakai, N.; Yokokawa, H.; Weber, A.; Ivers-Tiffée, E. *J. Electrochem. Soc.* **2001**, *148*, A456−A462.
(70) Primdahl, S.; Mogensen, M. *J. Electrochem. Soc.* **1999**, *146*, 2827−2833.
(71) Primdahl, S.; Mogensen, M. *J. Electrochem. Soc.* **1998**, *145*, 2431−2438.
(72) Bebelis, S.; Kotsionopoulos, N.; Mai, A.; Tietz, F. *J. Appl. Electrochem.* **2007**, *37*, 15−20.
(73) Hjalmarsson, P.; Sogaard, M.; Mogensen, M. *Solid State Ionics* **2009**, *180*, 1395−1405.
(74) Jamnik, J.; Maier, J. *Phys. Chem. Chem. Phys.* **2001**, *3*, 1668−1678.
(75) Kawada, T.; Suzuki, J.; Sase, M.; Kaimai, A.; Yashiro, K.; Nigara, Y.; Mizusaki, J.; Kawamura, K.; Yugami, H. *J. Electrochem. Soc.* **2002**, *149*, E252−E259.
(76) Benson, S. J. Ph.D. Dissertation, Imperial College: London, 1999.
(77) Fukuda, Y.; Hashimoto, S.-i.; Sato, K.; Yashiro, K.; Mizusaki, J. *ECS Trans.* **2009**, *25*, 2375−2380.